AIAA JOURNAL
Vol. 43, No. 8, August 2005

Planar Fluorescence Imaging of a Supersonic Axisymmetric Base Flow with Mass Bleed

Joel P. Kuehner*
Washington and Lee University, Lexington, Virginia 24450
and
J. Craig Dutton†
University of Texas at Arlington, Arlington, Texas 76019

Acetone planar laser-induced fluorescence (PLIF) was used to study the supersonic flow over an axisymmetric base with mass bleed. Detailed side-view and global end-view images were obtained in the recirculation regions, shear layer, and trailing wake. For the three bleed rates studied, the instantaneous behavior of the flowfield deviated substantially from the expected mean flow, especially for bleed rates below the optimal case. Large pockets of unmixed bleed fluid dominated the flowfield for the low and intermediate bleed rates, even in the trailing wake, highlighting the unsteady nature of the flowfield. The power-on condition for the high-bleed-rate case was the most temporally stable flowfield, due to the high momentum of the bleed jet. A multiplateau stirring effect was prevalent for all cases, consistent with previous compressible shear layer findings, and the effect increased with increasing bleed rate and distance downstream. Probability density functions (PDFs) of PLIF intensity indicated a similar mixing character between the low and intermediate bleed rates in the near wake and for all bleed rate cases in the trailing wake. The multiplateau stirring effect and unmixed bleed fluid pockets were represented well in the mixing PDFs.

Introduction

MANY practical aerodynamic flowfields, such as those for missiles and projectiles, involve a supersonic flow separating over an axisymmetric afterbody at a base corner. As with all base flows, a shear layer surrounding a recirculation region forms behind the object. The dynamics of separation, reattachment, and shear layer mass entrainment result in a pressure in the recirculation region that is lower than the freestream pressure. This low near-wake pressure, commonly referred to as base pressure, leads to substantial base drag on the body. For an object traveling near or beyond supersonic speeds, base drag comprises the primary contribution to the total drag force.[1] Therefore, an understanding of the physics governing the separated flow region and the resulting base pressure is necessary, so that modifications to the afterbody or other flow-control methods can be employed to increase base pressure and reduce the effects of base drag. This requires detailed knowledge of the dynamics of the turbulence present in the compressible free shear layer, recirculation region, and trailing wake. As a result, studies of the fluid dynamic mechanisms and interactions in these types of flows have been ongoing for many years now.[2]

Because of the compressible nature of the flow and associated potential wave-interference effects, the only reliable methods of investigation are nonintrusive diagnostic techniques. Initial studies of the baseline axisymmetric blunt-base case have been performed in which laser Doppler velocimetry (LDV)[3,4] was used to measure the mean velocity and turbulent stress fields. These studies were followed by planar Rayleigh Mie scattering (PRMS) visualizations (see Refs. 5 and 6) of the turbulent structures existing in the shear layer and near wake. Base-pressure fluctuations have also been investigated using high-speed pressure transducers mounted on the afterbody.[7] Additionally, experiments focused on altering the physics of the separation process and the recirculation region were performed to affect the magnitude of base drag present in the blunt-base case. Examinations of the effects of boattailing have shown an increase in base pressure,[7–9] whereas streamwise vorticity generation resulted in a decrease in base pressure.[10] Most recently, the use of an axisymmetric strip tab on the afterbody caused the base pressure to increase.[11]

Beyond these methods, changes in the recirculation region flow topology have been explored by introducing a central bleed jet through the base. This flowfield is shown schematically in Fig. 1 for the three bleed rate cases examined in this paper. The addition of the bleed jet alters the near-wake flow by supplying some or all of the mass entrained by the outer free shear layer. To characterize the amount of mass added to the recirculation region and the type of interaction that occurs with the shear layer, a nondimensional injection parameter I is used. This parameter is defined as the ratio of the bleed mass flow rate to the product of the freestream mass flux and base area. Without the bleed jet, there is a single, large recirculation region, and the forward stagnation point (FSP) resides on the base. As a small amount of bleed fluid is injected (Fig. 1a), the primary recirculation region (PRR), the FSP, and the rear stagnation point (RSP) are forced slightly downstream. A secondary recirculation region (SRR) forms as an annulus around the bleed jet, which, combined with the PRR, affects how the bleed flow interacts with the free shear layer. For this case, the added mass of the bleed flow partially fulfills the entrainment requirements of the shear layer and reduces the strength of the recompression shock system because less mass must be returned toward the base by the PRR. This, in turn, causes the base pressure to rise and reduces the magnitude of the base drag. This case, referred to here as case A, is in regime 1, where the bleed fluid accounts for only a portion of the mass entrainment requirements of the shear layer.

As the bleed rate is increased, the SRR grows in size and strength, the PRR decreases in size, and the FSP, RSP, and PRR all move downstream, as shown in Fig. 1b for case B. This case is nearing regime 2, in which the bleed flow supplies all of the shear layer entrainment mass, and the strength of the recompression shock system is minimized. Mathur[12] determined that regime 2 occurred at

Presented as Paper 2004-2650 at the AIAA Fluid Dynamics Conference, Portland, OR, 28 June–1 July 2004; received 3 September 2004; revision received 2 February 2005; accepted for publication 25 February 2005.

*Assistant Professor, Physics and Engineering Department. Member AIAA.

†Professor and Chair, Box 19018, Mechanical and Aerospace Engineering Department. Associate Fellow AIAA.

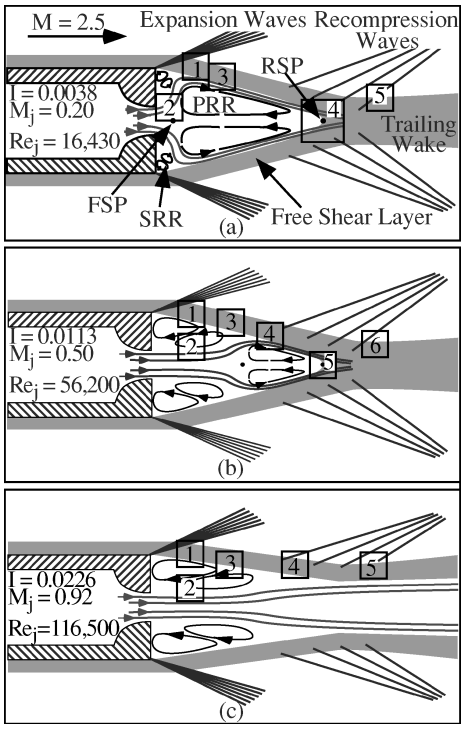

Fig. 1 Schematic of base-bleed flowfield three bleed rates: a) low, b) suboptimal, and c) postoptimal.

$I = 0.0148$ for the flow conditions studied here; therefore, case B is near optimal conditions in terms of maximum base pressure and minimum base drag. Finally, as seen in Fig. 1c, regime 3 begins as more mass is injected than can be entrained by the shear layer, and the PRR is eliminated by the momentum of the bleed jet, opening the wake. Case C, therefore, represents a power-on condition.

As was done for the blunt-base case, LDV[13,14] and PRMS imaging[15] were employed to study the base-bleed flowfield. Whereas PRMS provides images of the outer free shear layer and its structure, the interaction of the bleed jet with the PRR and SRR could not be investigated due to vaporization of the ethanol seed in these regions. Therefore, planar laser-induced fluorescence (PLIF) imaging of acetone seeded into the bleed jet was performed.[16] The PLIF images allowed the interaction of the bleed jet with various regions of the near-wake flow to be investigated.

In the previous PLIF base-bleed study,[16] global side-view images of the bleed jet were obtained, providing a basic insight into the large-scale flow structure. Unfortunately, detailed images of the bleed-jet interaction with the recirculation regions (PRR and SRR) and shear layer, as well as end views of the flowfield, were not acquired due to low signal levels. Thus, significant features of the flowfield were not imaged, leaving important elements of the physics of the base-bleed flowfield unaddressed.

Therefore, in this paper, we present a comprehensive PLIF imaging study of the base-bleed flowfield. With the use of an intensified charge-coupled device (CCD) camera, images of the essential detailed interactions in various local regions of the flowfield were captured. The fine circumferential structure of the shear layer has also been studied, so that further understanding of the effects of base bleed on the near-wake flowfield can be developed. Detailed side-view images are complemented with end views, which allow for the cross-stream flowfield structure to be investigated and radial variations of bleed jet mixing to be observed. Thus, the images and analysis presented in this paper provide a significant and important advancement in the understanding of the physics of a compressible axisymmetric base flow with a central bleed jet.

Experimental Facilities and Techniques

Flow Facility

The axisymmetric wind tunnel at the University of Illinois was used to perform these experiments and is presented in Fig. 2. Dry, high-pressure air is supplied to the stagnation chamber and then passes through an annular converging–diverging nozzle accelerating the flow to a nominal Mach number of 2.5. The stagnation pressure and temperature for these experiments were 512 kPa and 295 K, respectively, yielding a freestream unit Reynolds number of approximately 52×10^6 m^{-1}. The supply air flows over a centrally mounted cylindrical sting that supports the base-bleed afterbody. The afterbody has a diameter of 63.5 mm, and the bleed orifice has an exit diameter of 25.4 mm. The bleed flow is drawn in through the sting support from room air by the low base pressure that exists in the test section. This method of supplying the bleed mass avoids any acoustic issues associated with pressurizing the flow in a closed pipe. The volumetric flow rate of the bleed flow is throttled by a combination of butterfly and needle valves and is monitored by a Sierra 760 electronic flowmeter. The bleed flow is accelerated by a converging nozzle contained within the afterbody (Fig. 1) as it exits into the near wake. The stagnation temperature for the bleed flow was 297 K. The other experimental conditions for each case, based on the velocity measurements by Mathur,[12] are shown in Fig. 1.

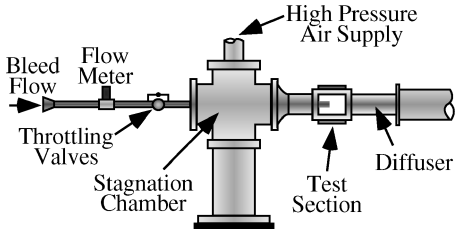

Fig. 2 Schematic of axisymmetric supersonic base-flow facility.

Acetone PLIF

Acetone PLIF has been demonstrated as an excellent means of imaging gaseous flowfields such as the base-bleed flow under consideration. Lozano et al.[17] demonstrated this fact by applying acetone as a tracer for high-speed flows. Since then, acetone PLIF has been applied in numerous flowfields, such as a transverse jet in crossflow,[18] a three-dimensional, turbulent freejet,[19] and a compressible free shear layer.[20] In addition to these applications, a detailed study of the temperature and pressure dependence of the acetone fluorescence signal was completed by Thurber et al.[21] and Thurber and Hanson.[22] Because of its dependence on the unknown thermodynamic conditions at the image locations in the current base-bleed flowfield, the acetone fluorescence intensity presented in this work can not be quantitatively related to bleed fluid mixture fraction. However, because the pressure and temperature should be nearly constant throughout the low-velocity recirculation regions, it is reasonable to assume that the fluorescence signal intensity represents the bleed mixture fraction qualitatively in those regions.

In the current experiments, acetone is seeded into the bleed jet by bubbling dry bottled air through a large bath of liquid acetone to ensure saturation at the exit. The saturated mixture is then injected into the bleed-jet intake, allowing it to mix with the induced room air before it reaches the test section. This bubbling method allows for consistent seeding levels, thereby eliminating a problem with previous measurements.[23] The spatial and temporal uniformity of this seeding method permitted the images to be processed and presented without applying image-to-image intensity corrections. For the experiments presented here, the acetone seeding level was approximately 1% of the bleed fluid by mass.

The vaporized acetone is excited using the 266-nm output of a quadrupled Nd:YAG laser (Continuum PL8010). The Nd:YAG laser provides approximately 80 mJ per pulse at a repetition rate of 10 Hz. The pulse length of the laser beam is between 6 and 8 ns and is, therefore, short enough to essentially freeze the features of the flowfield during image acquisition. The 266-nm beam is formed into a thin sheet (approximately 300 μm thick) using a series of lenses and is then directed into the test section with a final 266-nm turning mirror. The broadband, visible acetone fluorescence (350–550 nm) is imaged with an intensified camera (Princeton Instruments PI-MAX-512-T) that incorporates a 512×512 pixel CCD chip. Acetone has been shown to condense in the cold, high-speed

Table 1 Coordinates of the streamwise center of the image locations, x/R_{base}, parallel to centerline

Position	Case A	Case B	Case C
1	0.75	0.75	0.75
2	0.25	0.75	0.75
3	1.25	1.50	1.50
4	3.10	2.25	2.75
5	4.25	3.25	4.25
6	——	4.25	——

portions of the shear layer, starting at a distance approximately one base radius downstream from the base.[23] Because of the 266-nm excitation wavelength employed, the liquid acetone drops will contribute to the fluorescence signal; however, the size of the drops is expected to be small enough, that is, much less than the resolution of the imaging system, that the contribution will be negligible, based on the work of Bazile and Stepowski.[24] A 105-mm lens was used to focus the images onto the camera intensifier. Detailed side-view images were acquired by installing a 36-mm extension tube on the camera. End-view images were obtained obliquely through the facility side window and were rotated with software to eliminate perspective distortion. The f/stop was increased for the end-view images to increase the depth of field; however, the Scheimpflug condition was not strictly satisfied. Following the procedure of Clemens and Mungal,[25] the relative resolution of the imaging system was estimated, which relates the largest dimension of the probe volume, L, to the Batchelor mixing scale λ_B. For the images presented in this paper, the relative resolution is approximately 1000; as a result, the acetone signal does not represent mixing at the molecular scale, but rather at a larger stirring scale. Although underresolved in a molecular-mixing sense, this value of relative resolution is comparable to that in previous studies of similar flowfields.[25]

The image locations examined in the current study are shown in Fig. 1. Table 1 lists the distance downstream from the base for each location. All side-view images are 15 mm square, aside from case A, location 4, which is 25 mm square. Global end-view images were obtained at the streamwise midpoint of each side-view image location. The image ensemble at each location contains approximately 600 images. In the following discussion, image locations will be referred to with a letter indicating the case and the number of the image location labeled in Fig. 1. This paper will focus on three sets of image locations. Locations A1, B1, and C1 will be compared because they are at the same physical location in the flow. Locations A1, B3, and C4 are grouped because they are at the mean impingement points of the bleed jet on the outer shear layer for each case. The mean impingement point is defined here as the end of the SRR. Finally, locations A5, B6, and C5 are discussed together because they represent the start of the trailing wake, and they are also at the same physical location in the flowfield. Because of the similarities between the trailing-wake images for each case, images will be shown only for location A5 of this last group.

Results and Discussion

Case A: Low Bleed Rate

Sample instantaneous side-view images from location A1, at the mean bleed-flow impingement point, are shown in Figs. 3a and 3b. Figure 3c is a line plot of the acetone PLIF intensity values along the center column of each image, along with the intensity distribution of the center column of the ensemble-average image. This figure format will be used for all image locations shown herein. The large variability between the two images demonstrates that the instantaneous behavior of the near-wake flow deviates substantially from the mean flowfield, confirming the large-scale motions of the bleed jet seen in the previous global images for this low bleed-rate case.[16] These variations are highlighted by the line intensity plots (e.g., Fig. 3c). Figure 3a shows that the SRR (left) and PRR (right) might be distinguishable on an instantaneous basis, although this scalar image does not allow for a definitive determination.

Large pockets of unstirred bleed fluid, appearing as high signal regions, exist in the near wake at this location, as the bleed jet

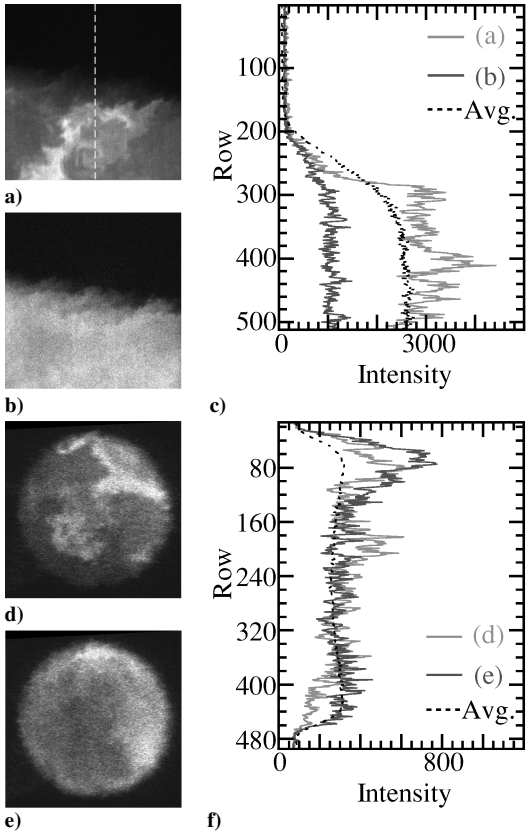

Fig. 3 Instantaneous images from location A1, mean impingement point for case A: a) and b) side view, d) and e) end view, and c) and f) intensity along center column of each image and ensemble average.

is forced up against the free shear layer. In Fig. 3b, the relatively uniform acetone signal would seem to imply that the bleed fluid has been well stirred at this particular instant; however, this is most likely not the case in a global sense. As seen in previous global side-view images,[16] large pockets of relatively unstirred bleed fluid probably do exist at this instant, but are out of the particular circumferential plane imaged here. This possibility will be further illustrated by the end-view images discussed later.

Where the acetone PLIF signal decreases toward the middle and top of the images, the inner, subsonic edge of the outer free shear layer is captured. Along this boundary, relatively small-scale structures dominate the shear layer, and it appears that they are generally elliptic and inclined toward the downstream direction. While large pockets of unstirred bleed fluid exist in the near wake at this location, corresponding large pockets of dark freestream fluid do not appear to be engulfed into the shear layer. The structure sizes and orientations are similar to those seen in PRMS images of the outer edge of the shear layer.[15] An important difference between these images and those of the PRMS study is seen at this location. Long strands of bleed fluid do not appear to extend upward toward the high-speed side of the shear layer, therefore, not replicating the strands seen extending from the freestream into the shear layer seen in the PRMS images. This seems to indicate that the inner portion of the shear layer imaged here does not contain rollerlike structures with thin braids between, as the outer edge does,[25] or that such structures are smaller than those on the outer edge of the shear layer and, hence, unresolved here.

Figures 3d and 3e contain instantaneous end-view images, and Fig. 3f shows the corresponding line intensity plots from location A1. The average intensity in these images is lower than for the side views, which is expected because of the oblique perspective from which the images were obtained. As was suggested by the global side-view images,[16] the bleed fluid is distributed relatively randomly about the cross section, such that the large-scale unsteady motion of the bleed jet is captured. This confirms the earlier conclusion that the relatively uniform intensity distribution in Fig. 3b is most

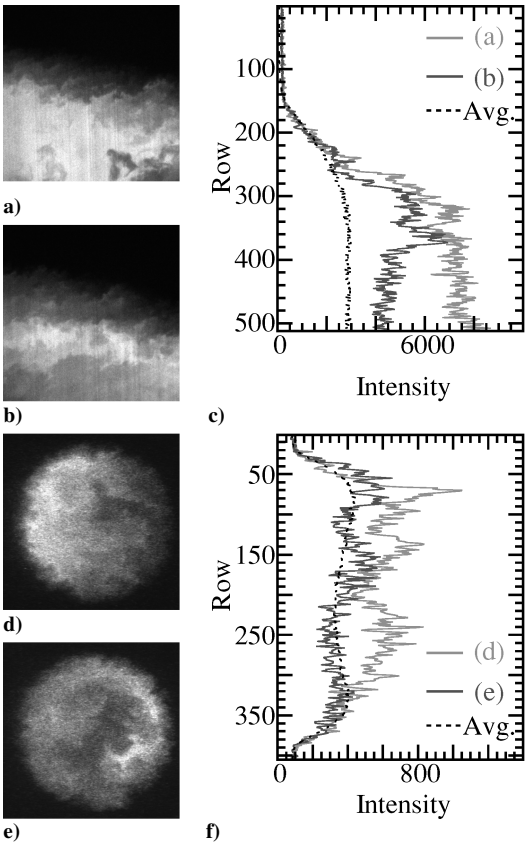

Fig. 4 Instantaneous images from location A3, near-wake shear layer for case A: a) and b) side view, d) and e) end view, and c) and f) intensity along center column of each image and ensemble average.

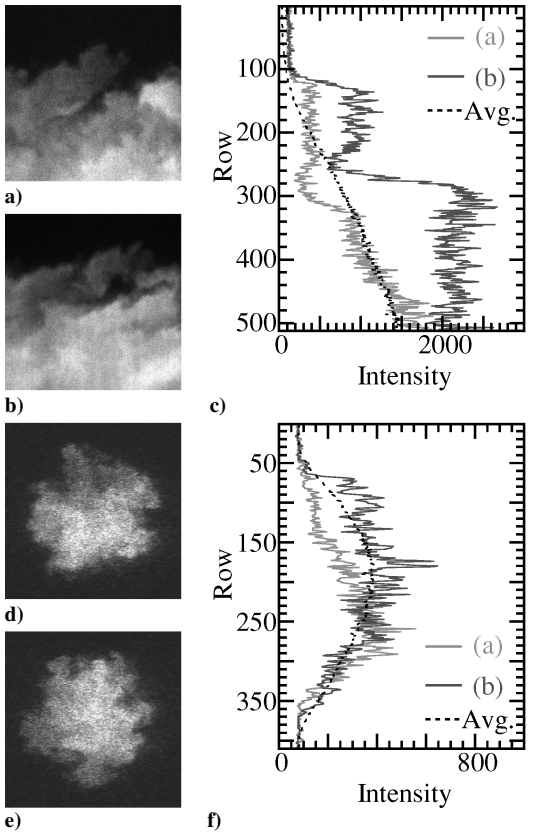

Fig. 5 Instantaneous images from location A5, trailing wake for case A: a) and b) side view and d) and e) end view, and c) and f) intensity along center column of each image and ensemble average.

likely not indicative of a well-stirred condition globally, but rather that the unmixed bleed jet exists at another circumferential position at that instant. The dark PRR that is expected at the center of the end-view images based on time-averaged flow considerations is not always instantaneously centered (Fig. 3e), nor is it always discernible (Fig. 3d). As seen in the line intensity plots in Fig. 3f, the average intensity distribution is very symmetric across the cross section, whereas the instantaneous line plots rarely are. Although the bleed fluid is not instantaneously symmetrically dispersed in the end-view images, the images are nominally circular at each instant. The turbulent structures at the outer edge of the images are relatively small, which corresponds well with the structures seen in the side-view images. This is also in agreement with the PRMS images of the outer portion of the shear layer at this location.[15]

Moving to location A3, shown in Fig. 4, changes in the structure of the shear layer and PRR with downstream position can be examined. As can be seen in the side-view images in Figs. 4a and 4b, large pockets of unstirred bleed fluid are still evident, although they appear larger in size than at location A1. The small-scale turbulent structures at the edge of the shear layer have grown in size, and a multiplateau effect in the image intensity distribution becomes noticeable in the cross-stream direction, as best seen in Fig. 4a. This is slightly more distinguishable in the line intensity plot (Fig. 4c) for the image, where there are two different intensity levels of stirring. This effect becomes more prominent with increased bleed rate and increased distance downstream, as will be discussed. The end-view images (Figs. 4d and 4e) are similar to those at location A1, with the bleed fluid being dispersed relatively arbitrarily around the periphery. The turbulent structures located at the edge of the end views, which were very small at location A1, have grown and are more perceptible here. The cross section of the end-view images is still very circular at this location, and the line intensity plot (Fig. 4f) for the ensemble average is again symmetric.

Figures 5a and 5b contain side-view results from the trailing wake, location A5. As expected from previous studies,[15,16] the structures at the edge of the images along the outer shear layer have grown markedly from location A1, are generally elliptic in shape, and are inclined in the streamwise direction. However, the structures appear smaller than those seen in the PRMS images,[15] implying a difference in the turbulent structures from the outer, supersonic edge to the inner, subsonic edge of the shear layer. Even at this distance downstream, pockets of relatively unstirred bleed fluid still exist at the lower edge of the images (Figs. 5a and 5b), indicating that the flowfield is still not completely mixed on an instantaneous basis. This is also confirmed by the shot-to-shot variation seen in the line intensity plots (Figs. 5c and 5f). Areas of engulfed dark freestream fluid are now present in the trailing wake, as shown in both side-view images (Figs. 5a and 5b). The multiplateau stirring effect seen at location A3 has become more noticeable, as demonstrated in Fig. 5b and the corresponding line intensity plot in Fig. 5c. Two distinct levels of intensity exist, indicative of multiple layers of structures interacting within the shear layer. This behavior has been previously found in high-convective Mach number free shear layers, where overlapping, slanted structures dominated the mixing physics.[25]

The trailing wake end-view images in Figs. 5d and 5e are noticeably different from those at locations A1 and A3, which were located before the end of the PRR. Here the wake cross section includes a bright, nominally centered portion with large turbulent structures dominating the edge. The instantaneous distribution of bleed fluid is no longer approximately circular, and the mean intensity distribution exhibits a small asymmetry. The mean asymmetry is most likely due to an artifact of the test section geometry.[23] Although the instantaneous behavior at this downstream location deviates significantly from the mean, the variations are not as stark as at locations A1 and A3 because the flow is relatively better mixed this far downstream.

Figure 6 contains the radial distribution of the rms intensity normalized by the mean intensity for the center column of the ensembles of side-view images at locations A1, A3, and A5. There is a peak in rms intensity at the same nominal location as the shear layer for each position. The change in peak locations does not imply lateral shear layer movement with downstream distance because the images are not located at the same radial locations in the flowfield (Fig. 1). The

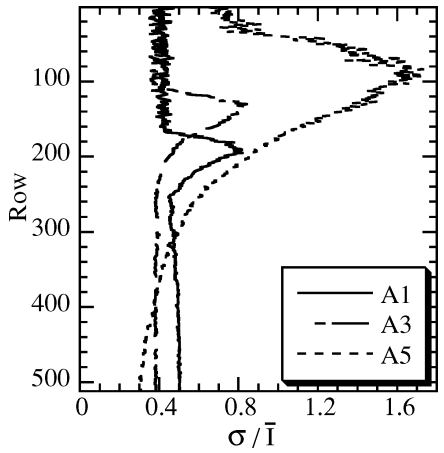

Fig. 6 Normalized rms intensity along center column of ensemble at locations A1, A3, and A5.

rms intensity in the near wake, locations A1 and A3, is similar to that seen in the global images of the previous study.[16] However, the peak seen at location A5 is almost an order of magnitude larger than in the previous findings. This stark increase is most likely due to the increased signal strength and resolution that the detailed side-view images of the current work provide. Pockets of unstirred bleed fluid and regions of engulfed freestream fluid are better resolved and, therefore, contribute more strongly to the rms statistics at this downstream location. This large rms intensity illustrates the degree of unmixedness in the trailing wake for case A. Whereas the peak rms intensity increases with downstream distance, the peak shape remains fairly uniform. The long tail toward the bottom of the profile is indicative of occurrences of large pockets of unstirred bleed fluid, which increase the perceived width of the shear layer.

Case B: Intermediate Bleed Rate

Side-view images obtained in the early shear layer for case B, location B1, are shown in Figs. 7a and 7b. This is the identical physical location as for A1 but is upstream of the mean bleed flow impingement point on the shear layer for this case. The increased signal as compared to that for location A1 is due to the increased amount of bleed fluid in the near wake. Unstirred pockets of bleed fluid, possibly larger than those at location A1, are again relatively randomly distributed across the images, although perhaps concentrated more in the lower left corner (Figs. 7a and 7b). Although the multiplateau stirring effect was not seen at location A1, it already appears at this location for case B; see, for example, the line intensity plot (Fig. 7c) corresponding to Fig. 7b. The structures at the edge of the shear layer are roughly the same size as those at location A1, which was also found in the PRMS images[15] of the outer portion of the shear layer. This is due to the similarity between the blunt-base, no-bleed case and all bleed rates at this location close to the base. However, compared to location A1, strands of bleed fluid are now seen extending upward into the shear layer. This difference between the cases was not discernible in the PRMS imaging study.[15]

With regard to the end views in Figs. 7d and 7e, the images are similar in nature to those at location A1. Figure 7e shows how different the flowfield can be from the mean, whereas Fig. 7d shows that the PRR can occasionally appear instantaneously centered at this location. The average line intensity plot (Fig. 7f) is symmetric, as it was for location A1.

Imaging results for the mean bleed fluid impingement point for case B, location B3, are shown in Fig. 8. For the side views (Figs. 8a and 8b), the region inside of the shear layer at the bottom of the images looks similar to that at location A1, especially the sizes of the unstirred pockets of bleed fluid. However, the outer edge of the shear layer itself is similar to that at location A3 due to the downstream distance of the image location. The turbulent structures seen at location B1 have grown, and the multiplateau stirring effect is more evident; see Fig. 8b. The distribution of bleed fluid over the inner portion of the end views (Figs. 8d and 8e) appears comparable to that

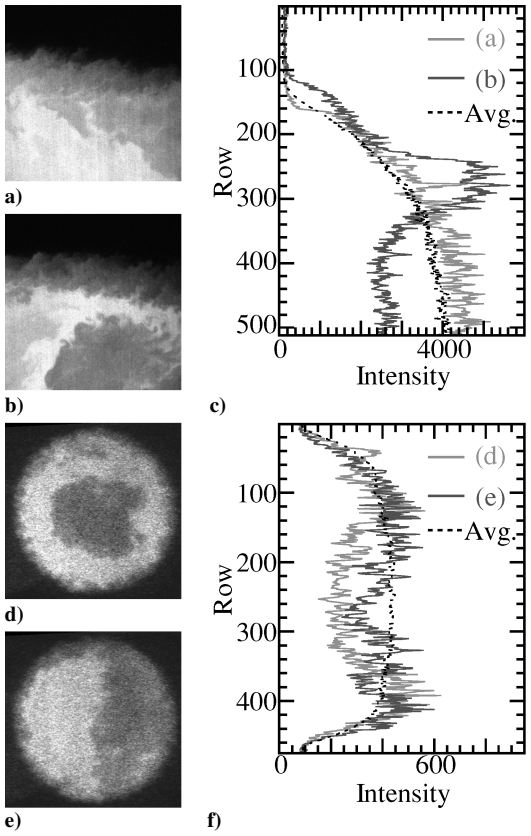

Fig. 7 Instantaneous images from location B1, early shear layer for case B: a) and b) side view, d) and e) end view, and c) and f) intensity along center column of each image and ensemble average.

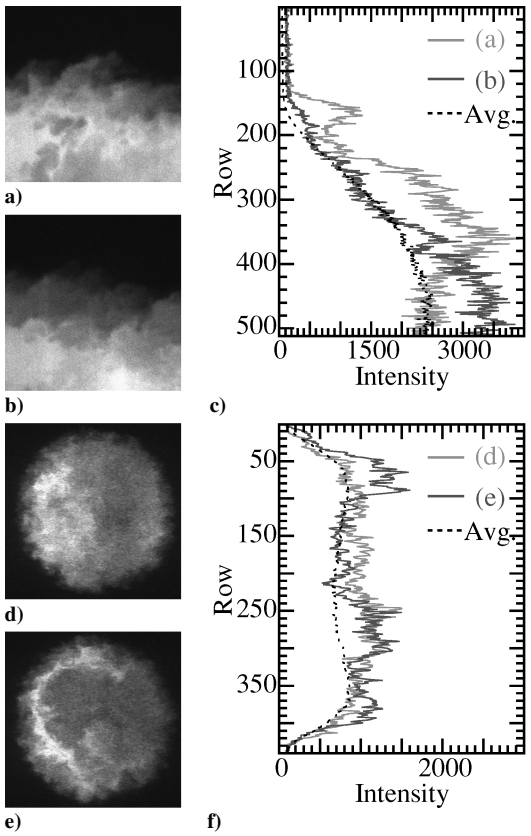

Fig. 8 Instantaneous images from location B3, mean impingement point for case B: a) and b) side view, d) and e) end view, and c) and f) intensity along center column of each image and ensemble average.

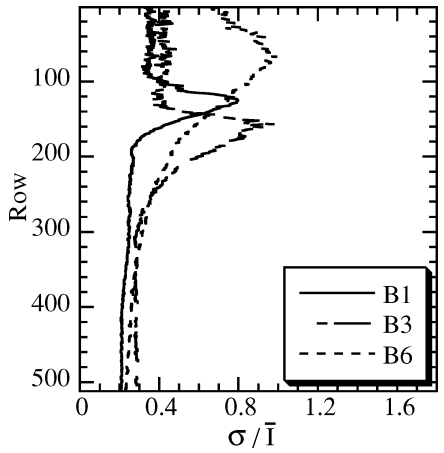

Fig. 9 Normalized rms intensity along center column of ensemble at locations B1, B3, and B6.

at both locations A1 and A3. The structures at the outer edge of the end views are analogous to those at location A3 but larger due to the increased downstream distance. The radial symmetry of the mean intensity distribution observed in the end views at locations A1, A3, and B1 continues at this location.

The change in normalized rms intensity with downstream distance is shown in Fig. 9 for case B. Overall, the profiles are similar in shape to those for case A (Fig. 6). However the peak intensity in the trailing wake, location B6, is not nearly as significant as for case A, location A5. This indicates that the flowfield is better mixed in the trailing wake for case B compared to case A. However, the rms intensity is still twice that found in the global images in the previous study,[16] again highlighting the effects of the increased resolution and signal strength of the current study.

Case C: High Bleed Rate

Figures 10a and 10b present side-view images of the early portion of the shear layer of case C, location C1. The average intensity is lower than at locations A1 and B1 because the SRR dominates this image location rather than unstirred pockets of bleed fluid, which occur less frequently now. Because of this reduced frequency, the instantaneous behavior varies less about the mean than for cases A or B at this location. This is confirmed by the line intensity plots in Fig. 10c, which show relatively small variations about the mean, that is, the flow is well mixed. The strands of bleed fluid seen at location B1 projecting up into the shear layer are also evident at location C1, indicating little change in the mixing physics between the cases at this location. The multiplateau stirring effect occurs here to some extent, although it is difficult to notice in the images due to the low intensity of the second plateau. The end-view images in Figs. 10d and 10e are strikingly different from those at location A1 or B1. Because the bleed fluid is a high-momentum, well-defined jet for this bleed rate, it is clearly evident near the center of the images, even with the low signal level (Figs. 10d and 10e). The bleed jet is typically round in the instantaneous images, as are the end-view cross sections in general. The line intensity plots display the steadiness of the bleed jet at this location (Fig. 10f).

Moving farther downstream to the mean impingement point (end of the SRR) at location C4 for this bleed rate, there is a noticeable change in shear layer behavior. As seen in the side-view images of Figs. 11a and 11b, the structures have grown dramatically due to the distance downstream, and there is an increased amount of engulfed freestream fluid present (Fig. 11a). In contrast to the other cases, the multiplateau effect can encompass three levels of stirring at location C4, as seen in Fig. 11c, the line plot for Fig. 11a. Whereas large isolated pockets of relatively unstirred bleed fluid do not exist in these images (Figs. 11a and 11b), large bands of bleed fluid usually reside at the bottom of the image. The behavior at the mean impingement point for this high-bleed case is noticeably different than that for case A, A1, and case B, B3. This is most likely because there is no

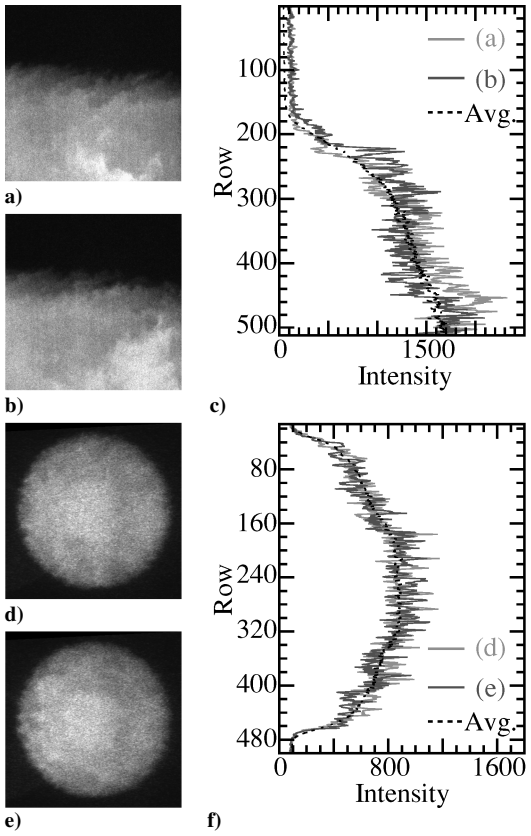

Fig. 10 Instantaneous images from location C1, early shear layer for case C: a) and b) side view, d) and e) end view, and c) and f) intensity along center column of each image and ensemble average.

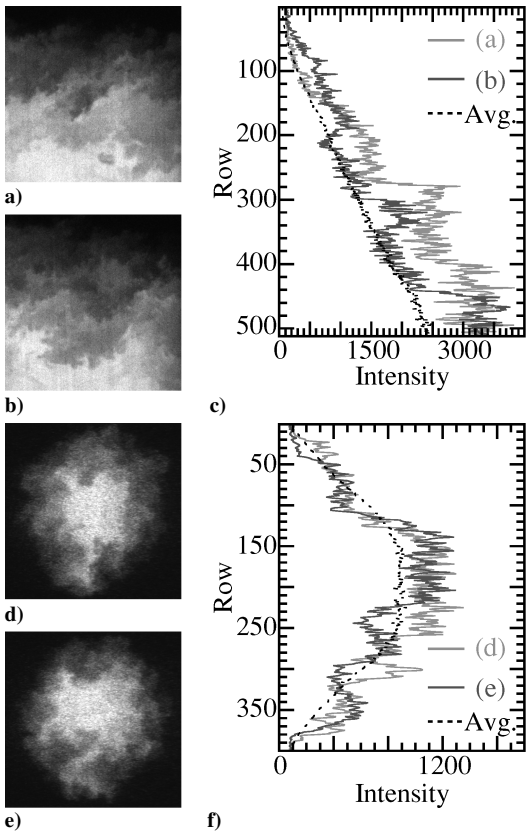

Fig. 11 Instantaneous images from location C4, mean impingement point for case C: a) and b) side view, d) and e) end view, and c) and f) intensity along center column of each image and ensemble average.

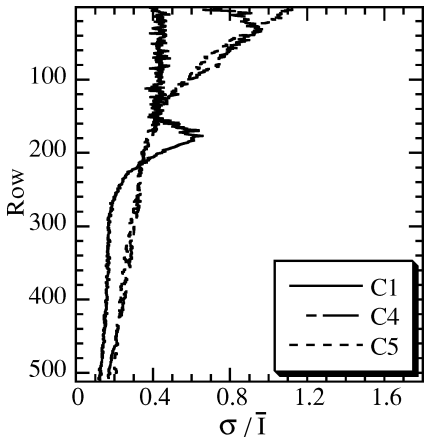

Fig. 12 Normalized rms intensity along center column of ensemble at locations C1, C4, and C5.

PRR for case C, and therefore, the physics of the flowfield are fundamentally different because the bleed fluid does not impinge strongly on the shear layer. At this distance downstream, the flowfield more closely resembles a supersonic jet in coflow, similar to the low convective Mach number coflowing jet studied by Bryant and Driscoll.[26]

The end views in Figs. 11d and 11e are similar to those of the trailing wake of case A, location A5 because the imaging positions are closely spaced physically. The central, bright bleed jet is surrounded by very large-scale structures at the periphery. As was seen at location C1, the bleed jet produces a uniform central region in the line intensity plots (Fig. 11f).

Figure 12 shows the normalized rms intensity for the side-view images of case C. The shapes of the profiles are roughly similar to those seen for cases A and B. However, the profile for the trailing wake, location C5, is not entirely captured due to the large radial motions of the shear layer and the possible increase in shear layer thickness here. It appears that the peak normalized rms intensity occurs near the outer edge of the shear layer at this location, rather than more centered in the layer, as would be expected.

Probability Density Functions

To provide a qualitative mixing comparison of the cases, probability density functions (PDFs) of the intensity realizations have been compiled. To increase the number of realizations in the PDFs, a three by three square of pixels was binned around each location and each PDF is divided into 50 bins. To verify that binning pixels would not bias the character of the mixing presented, PDFs were also assembled in which no binning was performed. It was found that the binned PDFs reduced the noise seen in the unbinned PDFs, but did not alter the fundamental PDF shapes. For the side views, the PDFs were constructed for the center column. Distance across the image will be referenced as follows: 0 will indicate the top of the image and 1 the bottom of the image, with fractions thereof. For the end views, the PDFs were created following the line from the center of the mean image down to the maximum radius of the mean image, R, with fractions thereof. Because of the large physical area considered for each realization, that is, conglomerate pixel size, these PDFs are not indicative of the mixture fraction at the Batchelor scale, rather they are a means of illustrating the qualitative behavior of macroscopic stirring at each location. Additionally, binning the pixels relaxes the Scheimpflug condition requirements for the end-view images because the sharpness of focus affects the resulting PDFs less significantly.

Figure 13 displays the PDFs for the side-view mean impingement points for each case. At location 0 in Fig. 13a, the PDF is heavily weighted at zero intensity because it is dominated by the dark freestream. (See Fig. 3 for example instantaneous images.) Down at the one-quarter location, the PDF does not change because it is still in the freestream. By the one-half location, however, the PDF has marched to the right and has a small right-side tail of high-intensity realizations. This tail is indicative of the large pockets of

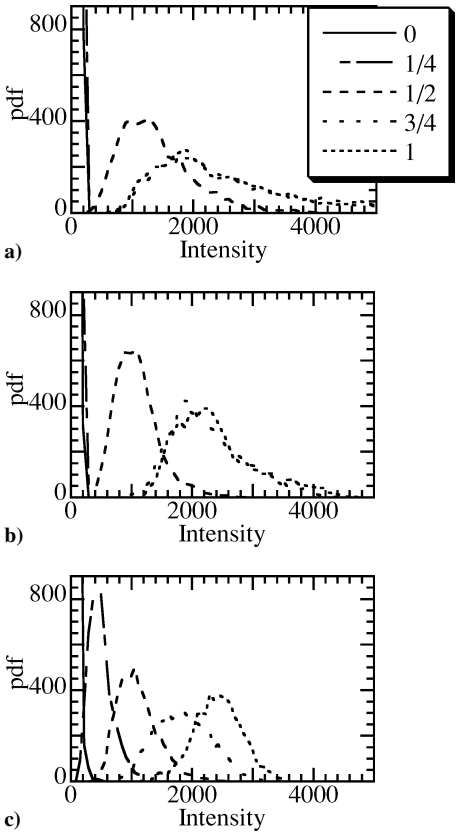

Fig. 13 PDFs of intensity along center column of the side-view image ensemble at mean impingement point for a) case A, location 1; b) case B, location 3; and c) case C, location 4.

unstirred bleed fluid that pass through the images (Fig. 3). At the three-quarter locations, the PDF has marched again to the right to higher-intensity realizations, the PDF has broadened, and the high-intensity tail has grown, representing a change in the character of stirring from the one-half to three-quarter locations. Moving down to location 1 of Fig. 13a, at the bottom of the images, the PDF is nearly identical to that at the three-quarter location, demonstrating that there is no change in the stirring behavior between these two positions. Figure 13b for the intermediate-bleed case shows that the stirring characteristics are largely similar between cases A and B at the mean bleed fluid impingement locations. However, the PDFs for case B are narrower than for case A. This represents somewhat better mixing for case B than case A because there are fewer high-intensity realizations of unstirred bleed fluid. Finally, as expected from the nature of the instantaneous images, the PDFs for high-bleed case C in Fig. 13c are obviously different than those for cases A or B. The PDFs are more Gaussian and march to increasingly higher intensity values the entire way across the images. The flat-top behavior seen in the PDF of Fig. 13c at the three-quarter location possibly signifies the multiplateau stirring effect noted in the instantaneous images (Figs. 11a and 11b) and line intensity plots (Fig. 11c).[25]

Moving to the PDFs for the side-view images in the trailing wake, Fig. 14 shows distinctly different stirring characteristics from those seen at the mean impingement point. The PDFs for all cases are more Gaussian in shape and march to higher intensity values from the top to the bottom of the images in all cases (Fig. 14). The flat-top behavior is now observed in more of the PDFs, which is consistent with the hypothesis that this feature represents the multiplateau stirring effect. Beyond the PDFs for intermediate-bleed case B being wider, the similarity between all cases at this location implies that bleed rate has only a marginal effect on the mixing and turbulence characteristics this far downstream. However, as shown by the rms intensity plots for cases A (Fig. 6) and B (Fig. 9), there are effects of bleed rate on the level of mixing in the trailing wake.

The PDFs for the end-view images at the mean impingement point are shown in Fig. 15. For case A (Fig. 15a), the PDFs do not march

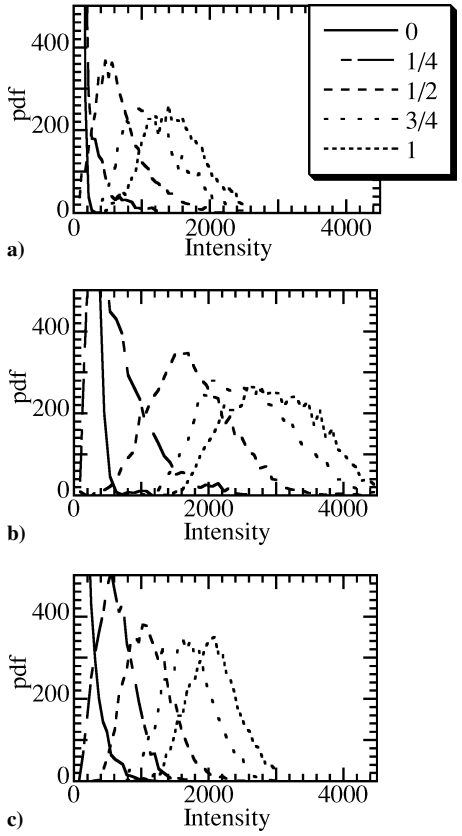

Fig. 14 PDFs of intensity along center column of side-view image ensemble in trailing wake for a) case A, location 5; b) case B, location 6; and c) case C, location 5.

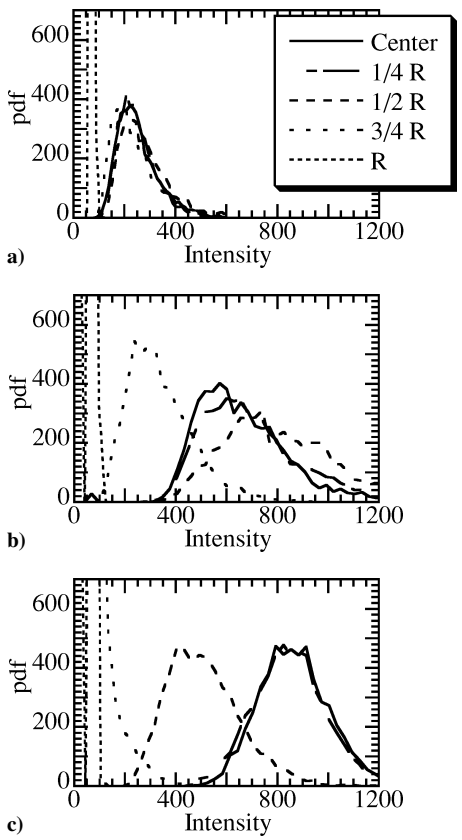

Fig. 15 PDFs of intensity along radius of end-view image ensemble at mean impingement point for a) case A, location 1; b) case B, location 3; and c) case C, location 4.

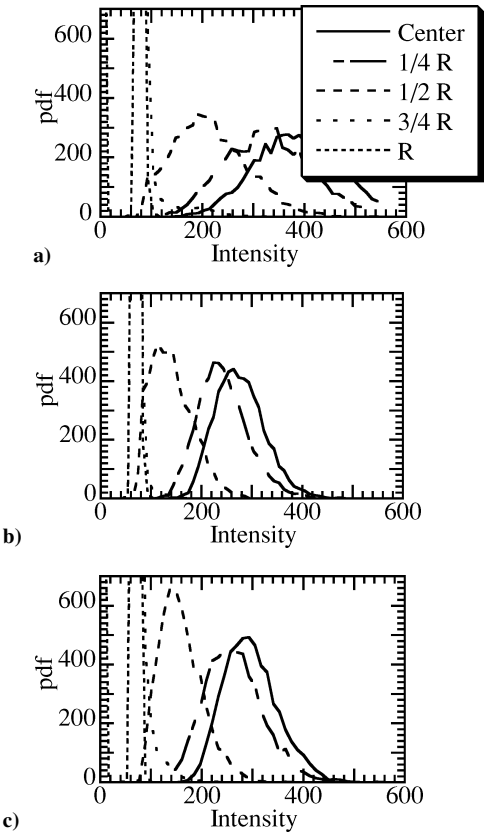

Fig. 16 PDFs of intensity along radius of end-view image ensemble in trailing wake for a) case A, location 5; b) case B, location 6; and c) case C, location 5.

until the edge of the end view (*R* location), which is most likely due to the random motion of the bleed jet at this location for the low bleed rate, rather than the PDFs indicating a well-stirred state. This is confirmed by the right tails on the PDFs, which represent pockets of relatively unstirred bleed fluid at all locations. The PDFs for intermediate-bleed case B (Fig. 15b) march slightly toward higher and then lower intensity values as the radial position is increased but still have the right tail. This marching trend is indicative of the image being centered near the FSP and the bleed fluid being forced around the nascent PRR. On the other hand, the PDFs for high-bleed case C (Fig. 15c) are more Gaussian in shape and generally march toward lower intensity values as the radial position is increased.

As was seen for the PDFs of the side-view images in the trailing wake (Fig. 14), the end-view PDFs (Fig. 16) are qualitatively very similar from case to case. The only difference between the PDFs for the various bleed rates is the wider PDFs seen for low-bleed case A, demonstrating that there is a wider range of intensity values that occurs for this low-bleed rate, that is, a smaller amount of mixing. This, along with the wider PDFs for case B in Fig. 14 and the rms intensity plots (Figs. 6, 9, and 12), implies that there is a small difference in the stirring characteristics in the trailing wake for the various bleed rates that was not immediately discernible from the instantaneous PLIF images. This difference may be related to the change in the number of structures at the edge of the shear layer seen in the end-view images of the PRMS study.[15] However, the change in structure number was not evident in the current PLIF end views. This result combined with the lack of bleed fluid strands seen at location A1 as compared to locations B1 and C1 and the multiplateau stirring effect observed at location B1 and then location C1, neither of which was evident in the PRMS study, indicates a possible difference between the high- and low-speed sides of the shear layer.

Conclusions

Acetone PLIF imaging was used to study the near-wake region of a supersonic flow over an axisymmetric afterbody with mass bleed. Detailed side-view and global end-view images allowed

examination of the turbulent structure and mixing characteristics for three different bleed rates. The results are compared to PRMS images of the outer edge of the shear layer,[15] and comparisons are made between the cases presented here, as well. For the edge of the shear layer, the trends seen in previous PRMS imaging studies of supersonic flow over an axisymmetric afterbody[5,6,8,10,11,15,16] are similar to those observed here. Most notably, the turbulent structures are generally elliptical, inclined toward the freestream, and grow with downstream distance. In contrast to the PRMS images, acetone PLIF imaging provides a detailed assessment of the flow structure in the recirculation regions. The violent sloshing of the low-momentum bleed fluid seen in the low-bleed case A images (Figs. 3–5) illustrates that the flowfield is highly unsteady and rarely approximates the features of the time-averaged flowfield. Large pockets of bleed fluid remain relatively unmixed from early in the shear layer, through recompression, and into the trailing wake. These pockets dominate the side- and end-view images and statistics at all locations for case A, aside from the end view in the trailing wake. This unsteadiness captured in the images illustrates that, although mean flowfield calculations have been able to reproduce time-averaged flowfield measurements, the calculations lack the actual random, instantaneous behavior that occurs in the flowfield.

For case B, the increase in bleed rate, and therefore momentum of the bleed fluid, has a stabilizing effect on the relatively arbitrary motions of the bleed fluid seen at the low-bleed rate. However, pockets of unstirred bleed fluid still exist at all locations, similar to case A. The behavior at the mean bleed fluid impingement point inside the shear layer (bottom of images at location B3 in Figs. 8a and 8b) is similar to that of the same region for case A (location A1). This implies that the mixing physics in this region, that is, size, number, and location of unstirred bleed fluid pockets, are not strongly dependent on the distance downstream. However, the shear layer characteristics at the outer edge of the images at the mean bleed fluid impingement point are different, due to the increased downstream distance of the impingement point for case B. The power-on condition examined in case C changes the flowfield behavior and corresponding images significantly. The large pockets of unstirred bleed fluid seen in cases A and B now become layers across the side-view images (Figs. 11a and 11b). The large-scale motion of the bleed fluid in the end view is also more contained due to the increased momentum of the bleed jet. The mixing and turbulence characteristics at the mean impingement point are markedly different than those for cases A and B due to the absence of the PRR.

Whereas downstream distance does not seem to affect the physics of the region inside the shear layer, it is clear that changes in bleed rate, which affect the downstream distance of the RSP, do modify the shear layer development, that is, size and orientation of structures. The multiplateau stirring effect was shown to appear at more upstream locations in the flowfield for increasing bleed rate. This indicates that the formation and interaction of turbulent structures in the outer shear layer are dependent on the effects of the bleed fluid on the recirculation regions (size of PRR and SRR) and RSP downstream distance, similar to the results found in the PRMS study.[15] The three-level plateau effect seen in case C highlights the changes with bleed rate by adding another tier of structures that appear to be interacting. Therefore, the detailed side-view and global end-view images presented and analyzed here provide new insight into the physics of the base-bleed flowfield, thereby enhancing the understanding obtained in previous studies.

Acknowledgments

This research was funded through the U.S. Army Research Office under Grant DAAD19-01-1-0367 with Thomas L. Doligalski as Technical Monitor.

References

[1]Sahu, J., Nietubicz, C. J., and Steger, J. L., "Navier–Stokes Computations of Projectile Base Flow with and Without Mass Injection," *AIAA Journal*, Vol. 23, No. 9, 1985, pp. 1348–1355.

[2]Dutton, J. C., "Compressible Turbulent Free Shear Layers," AGARD, Rept. R-819, Neuilly-Sur-Seine, France, June 1997.

[3]Herrin, J. L., and Dutton, J. C., "The Turbulence Structure of a Reattaching Axisymmetric Compressible Free Shear Layer," *Physics of Fluids*, Vol. 9, No. 11, 1997, pp. 3502–3512.

[4]Herrin, J. L., and Dutton, J. C., "Supersonic Base Flow Experiments in the Near Wake of a Cylindrical Afterbody," *AIAA Journal*, Vol. 32, No. 1, 1994, pp. 77–83.

[5]Bourdon, C. J., and Dutton, J. C., "Shear Layer Flapping and Interface Convolution in a Separated Supersonic Flow," *AIAA Journal*, Vol. 38, No. 10, 2000, pp. 1907–1915.

[6]Bourdon, C. J., and Dutton, J. C., "Planar Visualizations of Large-Scale Turbulent Structures in Axisymmetric Supersonic Separated Flows," *Physics of Fluids*, Vol. 11, No. 1, 1999, pp. 201–213.

[7]Janssen, J. R., and Dutton, J. C., "Time-Series Analysis of Supersonic Base-Pressure Fluctuations," *AIAA Journal*, Vol. 42, No. 3, 2004, pp. 605–613.

[8]Bourdon, C. J., and Dutton, J. C., "Effects of Boattailing on the Turbulence Structure of a Compressible Base Flow," *Journal of Spacecraft and Rockets*, Vol. 38, No. 4, 2001, pp. 534–541.

[9]Herrin, J. L., and Dutton, J. C., "Supersonic Near-Wake Afterbody Boattailing Effects on Axisymmetric Bodies," *Journal of Spacecraft and Rockets*, Vol. 31, No. 6, 1994, pp. 1021–1028.

[10]Bourdon, C. J., and Dutton, J. C., "Mixing Enhancement in Compressible Base Flows via Generation of Streamwise Vorticity," *AIAA Journal*, Vol. 39, No. 8, 2001, pp. 1633–1635.

[11]Bourdon, C. J., and Dutton, J. C., "Altering Turbulence in Compressible Base Flow Using Axisymmetric Sub-Boundary-Layer Disturbances," *AIAA Journal*, Vol. 40, No. 11, 2002, pp. 2217–2224.

[12]Mathur, T., "An Experimental Investigation of the Effects of Base Bleed in Axisymmetric Supersonic Flow," Ph.D. Dissertation, Dept. of Mechanical and Industrial Engineering, Univ. of Illinois, Urbana, IL, July 1996.

[13]Mathur, T., and Dutton, J. C., "Base-Bleed Experiments with a Cylindrical Afterbody in Supersonic Flow," *Journal of Spacecraft and Rockets*, Vol. 33, No. 1, 1996, pp. 30–37.

[14]Mathur, T., and Dutton, J. C., "Velocity and Turbulence Measurements in a Supersonic Base Flow with Mass Bleed," *AIAA Journal*, Vol. 34, No. 6, 1996, pp. 1153–1159.

[15]Bourdon, C. J., and Dutton, J. C., "Turbulence Structure of a Compressible Base Flow with a Central Bleed Jet," *Journal of Spacecraft and Rockets*, Vol. 41, No. 3, 2004, pp. 451–460.

[16]Bourdon, C. J., and Dutton, J. C., "Visualization of a Central Bleed Jet in an Axisymmetric, Compressible Base Flow," *Physics of Fluids*, Vol. 15, No. 2, 2003, pp. 499–510.

[17]Lozano, A., Yip, B., and Hanson, R. K., "Acetone: a Tracer for Concentration Measurements in Gaseous Flows by Planar Laser-Induced Fluorescence," *Experiments in Fluids*, Vol. 13, No. 6, 1992, pp. 369–376.

[18]Smith, S. H., and Mungal, M. G., "Mixing, Structure and Scaling of the Jet in Crossflow," *Journal of Fluid Mechanics*, Vol. 357, 1998, pp. 83–122.

[19]Su, L. K., and Clemens, N. T., "Planar Measurements of the Full Three-Dimensional Scalar Dissipation Rate in Gas-Phase Turbulent Flows," *Experiments in Fluids*, Vol. 27, No. 6, 1999, pp. 507–521.

[20]Papamoschou, D., and Bunyajitradulya, A., "Evolution of Large Eddies in Compressible Shear Layers," *Physics of Fluids*, Vol. 9, No. 3, 1997, pp. 756–765.

[21]Thurber, M. C., Grisch, F., Kirby, B. J., Votsmeier, M., and Hanson, R. K., "Measurements and Modeling of Acetone Laser-Induced Fluorescence with Implications for Temperature-Imaging Diagnostics," *Applied Optics*, Vol. 37, No. 21, 1998, pp. 4963–4978.

[22]Thurber, M. C., and Hanson, R. K., "Pressure and Composition Dependences of Acetone Laser-Induced Fluorescence with Excitation at 248, 266, and 308 nm," *Applied Physics B*, Vol. 69, No. 3, 1999, pp. 229–240.

[23]Bourdon, C. J., "Flow Visualizations and Measurements of Turbulent Structures in Drag-Altered Axisymmetric Compressible Base Flows," Ph.D. Dissertation, Dept. of Mechanical and Industrial Engineering, Univ. of Illinois, Urbana, IL, June 2001.

[24]Bazile, R., and Stepowski, D., "Measurements of Vaporized and Liquid Fuel Concentration Fields in a Burning Spray Jet of Acetone Using Planar Laser Induced Fluorescence," *Experiments in Fluids*, Vol. 20, No. 1, 1995, pp. 1–9.

[25]Clemens, N. T., and Mungal, M. G., "Large-Scale Structure and Entrainment in the Supersonic Mixing Layer," *Journal of Fluid Mechanics*, Vol. 284, 1995, pp. 171–216.

[26]Bryant, R. A., and Driscoll, J. F., "Structure of Supersonic Flames Imaged Using OH/Acetone Planar Laser-Induced Fluorescence," *AIAA Journal*, Vol. 39, No. 9, 2001, pp. 1735–1741.

R. Lucht
Associate Editor